

## Inertial settling of flexible fiber suspensions

Arash Alizad Banaei <sup>1</sup>, Mona Rahmani <sup>2</sup>, D. Mark Martinez,<sup>3</sup> and Luca Brandt <sup>1</sup>

<sup>1</sup>*Department of Mechanics, Linné Flow Centre, KTH, Swedish e-Science Research Centre,  
100 44 Stockholm, Sweden*

<sup>2</sup>*Department of Mathematics, The University of British Columbia, Vancouver,  
British Columbia, Canada V6T 1Z2*

<sup>3</sup>*Department of Chemical and Biological Engineering, The University of British Columbia, Vancouver,  
British Columbia, Canada V6T 1Z3*



(Received 13 June 2019; accepted 3 January 2020; published 5 February 2020)

We study the inertial settling of suspensions of flexible and rigid fibers using an immersed boundary method. The fibers considered are inextensible and slender, with an aspect ratio of 20. For a single Galileo number of  $Ga = 160$ , we examine a range of dimensionless bending rigidities  $0.1 < \gamma < 20$  and fiber concentrations  $0.5 < nL^3 < 25$ , with  $n$  being the fiber number density and  $L$  the fiber length, that spans dilute and semidilute regimes. The settling fibers form streamers, regions where the fibers are packed and settle faster than the average settling velocity of the suspension, for  $nL^3 > 10$ . In the low-concentration regions outside the streamers, the fibers either go upward or have low settling velocities. Flexible fibers exhibit higher packing inside the streamers and smaller streamers compared to the streamers formed by the rigid fibers. Due to this higher packing, the flexible fibers settle faster compared to the rigid fibers. The formation of the streamers counterbalances the hindering of the settling velocity at higher concentrations. At higher  $nL^3$ , however, the maximum local concentration of fibers relative to a uniform distribution diminishes for both flexible and rigid fibers as the mobility of the fibers becomes limited due to the presence of other fibers in their vicinity. Due to this limited mobility, the deformation of the fibers and their settling orientation become insensitive to  $nL^3$  for  $nL^3 > 7$ . In both the dilute and semidilute regimes, flexible fibers are more aligned with the direction perpendicular to gravity compared to rigid fibers.

DOI: [10.1103/PhysRevFluids.5.024301](https://doi.org/10.1103/PhysRevFluids.5.024301)

### I. INTRODUCTION

Sedimentation of fiber suspensions is present in many industrial processes and biological flows. In paper making, sedimentation of flexible fibers and their flocculation in the pulp suspension significantly influences the final structure of the paper [1]. Settling of flexible slender bodies is also important in the treatment of the pulp and paper mill wastewater [2], deposition of airborne particles with arbitrary flexible shapes in industrial clean rooms [3], and dispersion process of carbon nanotubes used as reinforcing fibers [4]. In biological flows, near the sea floor, settling is an important mechanism of transportation of microorganisms and organic material which commonly have slender flexible body shapes [5].

The settling behavior of flexible fiber suspensions is determined by an intriguing interaction between viscous, gravitational, elastic, and long-range hydrodynamic forces that depend on the fiber structure, aspect ratio, flexibility, density, and volume fraction of the suspension. These effects have been explored for fibers settling in viscous flows in several computational and experimental studies in the past. The settling speed of a single rigid fiber in a Stokes flow was theoretically derived by Batchelor [6] and updated by Mackaplow and Shaqfeh [7] using a slender body approximation.

These studies showed that unlike spheres in a Stokes flow, an isolated fiber can have a motion perpendicular to the gravity direction while maintaining its initial orientation while settling. The effects of fiber flexibility on the settling of an isolated fiber in Stokes flows have been studied theoretically [8,9], numerically [8,10–15], and experimentally [13] (see Ref. [16] for a recent review and the references contained therein). For weakly flexible fibers, the slender body theory of Xu and Nadim [9] showed that an isolated fiber settling in a viscous fluid experiences a torque that makes it reorient itself to the direction perpendicular to the gravity. In numerical simulations of settling of semiflexible fibers by Llopis *et al.* [12], the reorienting torque increased with increasing filament flexibility, implying that more flexible fibers adjust to the direction perpendicular to the gravity faster. Further studies [11,13] have established three regimes of fiber settling in Stokes flows depending on fiber flexibility. At low fiber flexibility, the fiber is weakly deformed and settles at velocities close to the settling velocity of a rigid fiber with an orientation perpendicular to the gravity direction. At high fiber flexibility, large fiber deformations occur, fiber height and end-to-end distance saturate to constants, and the settling velocity becomes close to that of a rigid fiber of half the original length settling vertically in a viscous flow. Recently, Marchetti *et al.* [13] proposed a model for the settling velocity of a single fiber at intermediate fiber flexibility. At very high fiber flexibility, fibers settling aligned with the gravity direction in a viscous fluid can become unstable to buckling [8], and fibers settling aligned with the direction perpendicular to the gravity can adopt shapes with more than one minimum, e.g., W shapes, although as pointed out by Marchetti *et al.* [13] W shapes are not stable. The instability of flexible fibers to buckling has also been addressed in shear flows [17,18], cellular flows [19,20], and extensional flows [21].

The hydrodynamic interaction of fibers in suspensions adds another complexity to the settling behavior of fibers. For suspensions of rigid fibers in a Stokes flow, Herzhaft and Guazzelli [22] identified two regimes depending on the fiber concentration, measured by  $n(L/2)^3$ , with  $n$  being the fiber number density and  $L$  the fiber length. For dilute regimes with  $n(L/2)^3 < 1$ , the settling velocity of the suspension was enhanced due to the formation of the streamers, regions of fiber clustering, and alignment of the fiber clusters with the gravity direction. In this regime, the average settling velocity of the suspension reached maximum values higher than the Stokes velocity of an isolated fiber. These results were similarly elucidated in the numerical simulations of Butler and Shaqfeh [23], Mackaplow and Shaqfeh [7], Saintillan *et al.* [24], and Tornberg and Shelley [17] and laboratory observations of Metzger *et al.* [25] and Salmela *et al.* [26]. For denser concentrations of the fibers, i.e.,  $n(L/2)^3 > 1$ , while the fibers still tended to orient to the direction of gravity, the effect of fiber streamers seemed to be weakened and the average settling velocity of the suspension was hindered [22].

The collective settling behavior of flexible fibers has received much less attention in the literature. For settling of two flexible fibers, Llopis *et al.* [12] showed numerically that the settling velocity and the shape of the settling fibers highly depend on the initial configuration and flexibility of the fibers. In their study, the hydrodynamic interaction of two fibers could cause more bending, rotation, translation, or collision of the two fibers. For a suspension of weakly flexible fibers in a Stokes flow, Manikantan *et al.* [27,28] showed analytically and numerically that fiber flexibility can both enhance clustering of the settling fibers by contributing to the anisotropy of the flow field and hinder clustering by reorienting the flexible fibers. While the hydrodynamic interaction of flexible fibers has been less explored in the case of settling fibers, suspensions of flexible fibers in shear flows have been examined in a few studies [17,29–31]. For example, for a suspension of flexible fibers in a shear flow, Tornberg and Shelley [17] showed that the fibers go through a periodic cycle of buckling and straightening. Numerical simulations of flexible fibers in turbulent channel flows have been carried out by Kunhappan *et al.* [32] and Dotto and Marchioli [33]. Both these studies revealed accumulations of flexible fibers near the walls. The interaction of flexible fibers with turbulence has been shown to highly depend on fiber length and flexibility [34,35].

Despite the widespread application of settling of flexible fibers in inertial regimes (see, e.g., [36]), most sedimentation studies of flexible fibers have been focused on low-Reynolds-number flows [16]. Our objective in the present study is to explore the settling and clustering of weakly and

moderately flexible fibers in an inertial regime for a range of dilute and semidilute concentrations. Similar to the studies by Herzhaft and Guazzelli [22], Mackaplow and Shaqfeh [7], and Salmela *et al.* [26], we are interested in identifying a transitioning settling behavior as the fiber number density increases from a dilute to a more concentrated regime. Our study, however, extends the results of these previous investigations to flexible fibers and also to an inertial regime. It is known that in inertial flows the drag force on flexible fibers is reduced due to large fiber deformations and streamlining of the flow [37,38] and inertial effects can induce an additional reorienting torque on a settling fiber [39]. However, the interaction of inertial effects and long-range hydrodynamic forces in a suspension of fibers, which is the subject of this paper, is still not well understood. We will use an immersed boundary method for the coupling between the fluid and fiber [18,40–42]. Other conventional methods for simulations of flexible fibers have been bead-rod models [10,11,13,43] and slender body theory [17,23,24,44,45], although the immersed boundary methods are more powerful for simulations of a suspension of thin fibers and especially in inertial regimes. We explain the numerical methods and their validation in Sec. II. We examine the formation of the streamers in suspensions of rigid and flexible fibers in Sec. III, the suspension settling in Sec. IV, the fiber deformation and orientation in Sec. V, with the conclusions stated in Sec. VI.

## II. NUMERICAL METHODS

### A. Fiber dynamics

We consider inextensible slender fibers. The dynamics of a thin flexible fiber can be described by the Euler-Bernoulli beam equation under the constraint of inextensibility, which in a dimensionless form is expressed as

$$\frac{\partial^2 \mathbf{X}}{\partial t^2} = \frac{\partial}{\partial s} \left( T \frac{\partial \mathbf{X}}{\partial s} \right) - \gamma \frac{\partial^4 \mathbf{X}}{\partial s^4} + \frac{1}{r} \frac{\mathbf{g}}{g} - \mathbf{F} + \mathbf{F}_c, \quad (1)$$

$$\frac{\partial \mathbf{X}}{\partial s} \cdot \frac{\partial \mathbf{X}}{\partial s} = 1, \quad (2)$$

where  $\mathbf{X}$  is the fiber position,  $s$  the curvilinear coordinate along the fibers,  $T$  the dimensionless tension,  $\gamma$  the dimensionless bending rigidity,  $\mathbf{F}$  the dimensionless fluid-solid interaction force per unit length,  $\mathbf{F}_c$  the dimensionless repulsive force used to model the interactions between adjacent fibers, and  $\mathbf{g}$  the gravitational acceleration vector with the magnitude of  $g$ . The parameter  $r$  quantifies the density ratio between the fluid and the fibers and is defined as  $r = \rho_l / (A_f \rho_0)$ , where  $\rho_l$  is the linear density difference between the fluid and the fibers,  $\rho_0$  is the density of the base fluid, and  $A_f$  is the cross-sectional area of the fibers.

Equations (1) and (2) have been nondimensionalized using the following characteristic scales:  $L$ , the initial length of fibers for the length scale;  $L/U_s$  for the timescale, where  $U_s = \sqrt{rgL}$  is a characteristic velocity scale;  $\rho_l U_s^2$  for tension; and  $\rho_l U_s^2 / L$  for the gravitational, fluid-solid interaction, and repulsive forces. Therefore, the dimensionless bending rigidity  $\gamma = EI / (\rho_l L^3 gr)$  measures the ratio of a convective timescale to an elastic timescale, with  $E$  being the Young's modulus and  $I$  the second moment of area. This definition implies that flexibility increases with decreasing  $\gamma$ . At the free ends of the fibers, we impose zero torque, zero force, and zero tension boundary conditions, i.e.,

$$\frac{\partial^2 \mathbf{X}}{\partial s^2} = 0, \quad \frac{\partial^3 \mathbf{X}}{\partial s^3} = 0, \quad T = 0. \quad (3)$$

### B. Flow field equations

We consider an incompressible suspending fluid, governed by the Navier-Stokes equations. In an inertial Cartesian frame of reference, the nondimensional momentum and mass conservation equations for an incompressible flow are

$$\frac{\partial \mathbf{u}}{\partial t} + \nabla \cdot (\mathbf{u} \otimes \mathbf{u}) = -\nabla p + \frac{1}{\text{Ga}} \nabla^2 \mathbf{u} + \mathbf{f}, \quad (4)$$

$$\nabla \cdot \mathbf{u} = 0, \quad (5)$$

where  $\mathbf{u} = (u, v, w)$  is the velocity field,  $p$  the pressure,  $\mathbf{f}$  a volume force (used to account for the suspended fibers), and  $\text{Ga} = \sqrt{rgL^3}/\nu$  the Galileo number, with  $\nu$  being the fluid kinematic viscosity.

We solve Eqs. (1) and (2) numerically using the two-step method proposed by Huang *et al.* [46] and with a finite-difference discretization. We solve a Poisson equation for the tension using a predicted position  $\mathbf{X}^* = 2\mathbf{X}^n - \mathbf{X}^{n-1}$ , where  $\mathbf{X}^n$  and  $\mathbf{X}^{n-1}$  are the solutions at previous times. To find the new position of the fibers at time  $t_{n+1}$ , the updated value of the tension  $T$  is used in Eq. (1). For the fluid, a second-order finite-difference method on a fixed staggered grid is used. The equations are advanced in time by a semi-implicit fractional step method, where the second-order Adams-Bashforth method is used for the convective terms, a Helmholtz equation is built with the diffusive and temporal terms, and all other terms are treated explicitly [47].

Fluid and solid motions are coupled using an immersed boundary method [48]. In this approach, there are two sets of grid points: a fixed Eulerian grid  $\mathbf{x}$  for the fluid and a moving Lagrangian grid  $\mathbf{X}$  for the fibers. The volume force  $\mathbf{f}$  arising from the action of the filaments on the fluid is obtained by the convolution of the singular forces estimated on the Lagrangian nodes onto the Eulerian mesh; these are computed using the fluid velocity interpolated at the location of the Lagrangian points. This interpolation/spreading is usually performed by means of regularized  $\delta$  functions, in our case the one proposed by Roma *et al.* [49]. The fluid and solid equations are linked together by a hydrodynamic force

$$\mathbf{F} = \frac{\mathbf{U}_{ib} - \mathbf{U}}{\Delta t}, \quad (6)$$

where  $\mathbf{U}_{ib}$  is the interpolated velocity on the Lagrangian points,  $\mathbf{U}$  is the velocity of the Lagrangian points, and  $\Delta t$  is the time step. The interpolation and spreading between the two grids are performed using the smooth  $\delta$  function introduced by Roma *et al.* [49],

$$\mathbf{U}_{ib} = \int_V \mathbf{u} \delta(\mathbf{X} - \mathbf{x}) dV, \quad (7)$$

$$\mathbf{f} = \rho \int_{L_f} \mathbf{F} \delta(\mathbf{X} - \mathbf{x}) ds, \quad (8)$$

where the factor  $\rho = \rho_l(\rho_0 L^2)$  arises from choosing different scales for Eulerian and Lagrangian forces.

To consider short-range interactions between fibers, we use the lubrication model proposed by Lindström and Uesaka [50]. The model is based on the lubrication force between two infinitely long cylinders in situations where the two cylinders are parallel or nonparallel. For the nonparallel case, Yamane *et al.* [51] derived a first-order approximation of the lubrication force

$$\mathbf{F}_1^l = \frac{-12}{\text{Ga} \sin \alpha} \frac{\dot{\mathbf{h}}}{h}, \quad (9)$$

where  $h$  denotes the shortest distance between the cylinders,  $\dot{\mathbf{h}}$  is the velocity along the shortest distance, and  $\alpha$  is the angle between the axis of the two cylinders. To use this approximation in the Euler-Bernoulli equations, the force is converted into a force per unit length, i.e., it is divided by  $\Delta s$ , the Lagrangian grid spacing. Equation (9) cannot be used to model the lubrication between parallel cylinders since  $\mathbf{F}_1^l \rightarrow \infty$  as  $\alpha \rightarrow 0$ . In this case, a first-order approximation of the force per unit length was derived by Kromkamp *et al.* [52],

$$\mathbf{F}_2^l = \frac{-4}{\pi \text{Gar}_p^2} \left( A_0 + A_1 \frac{h}{a} \right) \left( \frac{h}{a} \right)^{-3/2} \dot{\mathbf{h}},$$

$$A_0 = 3\pi\sqrt{2}/8, \quad A_1 = 207\pi\sqrt{2}/160, \quad (10)$$

TABLE I. Physical parameters defining the simulations performed. A total of 15 simulations were performed in which the Galileo number  $Ga$ , the fiber aspect ratio  $r_p$ , and the relative density ratio  $r$  were fixed while the bending rigidity  $\gamma$  and the fiber number density  $nL^3$  varied.

$Ga$	$r_p$	$\gamma$	$r$	$nL^3$
160	20	20, 0.5, 0.1	0.1	0.5, 3, 7, 10, 15, 25

where  $a$  is the radius of the cylinders ( $a = d/2$ ). Based on Eqs. (9) and (10), the following approximation of the lubrication force for two finite cylinders can be derived [50]:

$$\mathbf{F}^l = \min(\mathbf{F}_1^l / \Delta s, \mathbf{F}_2^l). \quad (11)$$

In our simulations, when the shortest distance between two Lagrangian point becomes lower than  $d/4$ , we impose the lubrication correction  $\mathbf{F}^{lc} = \mathbf{F}^l - \mathbf{F}_0^l$ , with  $\mathbf{F}_0^l$  the lubrication force at a distance of  $d/4$ . Finally, the total lubrication force acting on the  $i$ th element is obtained as

$$\mathbf{F}_i^{lc} = \sum_{j \neq i}^{nl} \mathbf{F}_{ij}^{lc}, \quad (12)$$

where  $nl$  is the number of Lagrangian points closer than the activation distance  $d/4$  to the  $i$ th point.

To avoid contact and overlap between fibers, a repulsive force is also implemented. This has the form of a Morse potential [53], with a general form

$$\phi = D_e [e^{-2\beta(r_f - r_e)} - 2e^{-\beta(r_f - r_e)}], \quad (13)$$

where  $D_e$  is the interaction strength,  $\beta$  a geometrical scaling factor,  $r_f$  the distance between two elements on two different fibers, and  $r_e$  the zero cutoff force distance. The repulsive force between the elements  $i$  and  $j$  is the derivative of the potential function  $\phi$ ,

$$\mathbf{F}_{ij}^c = \frac{d\phi}{dr} \mathbf{d}_{ij}, \quad (14)$$

where  $\mathbf{d}_{ij}$  is the unit vector in the direction joining the contact points. Finally, the total repulsive force on the  $i$ th element is obtained as

$$\mathbf{F}_i^c = \sum_{j \neq i}^{nc} \mathbf{F}_{ij}^c, \quad (15)$$

where  $nc$  is the number of Lagrangian points closer than the cutoff distance  $r_e$  to the  $i$ th point. As we consider moderate values of flexibility, we neglect the interaction of fibers with themselves. We also neglect contact frictional forces for all the cases in this study.

### C. Parameters and validation

The physical and numerical parameters of our simulations are summarized in Tables I and II, respectively. The Galileo number is chosen to be large enough to represent fibers with finite inertia. The bending rigidities of  $\gamma = 20, 0.5$ , and  $0.1$  correspond to rigid, weakly flexible, and moderately

TABLE II. Numerical parameters in the simulations performed.

Domain size $L_x \times L_y \times L_z$	Grid size $N_x \times N_y \times N_z$	Number of Lagrangian points per fiber	Time step
$2\pi \times 2\pi \times 4\pi$	$128 \times 128 \times 256$	21	0.0005

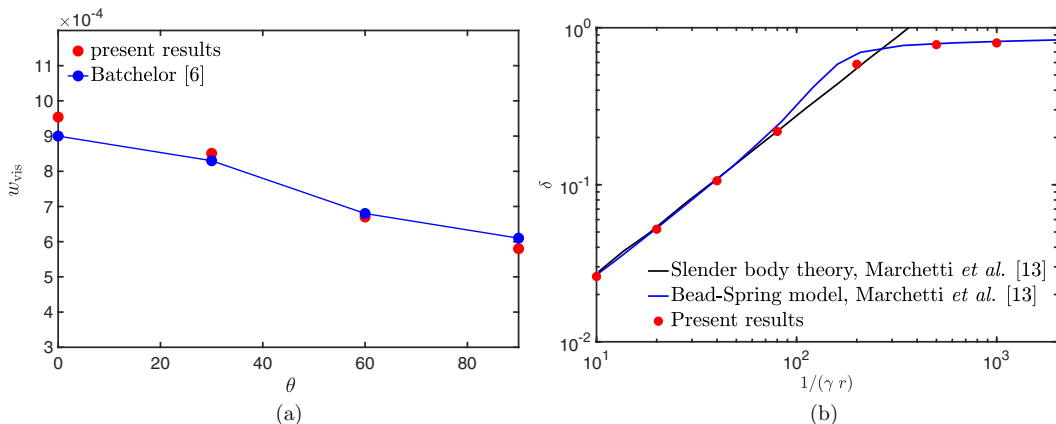


FIG. 1. (a) Averaged normalized settling velocity of a single rigid fiber at  $\text{Ga} = 1$  for different initial angles of the fiber with the gravity direction and comparisons to the analytical solution of Batchelor [6] given in Eq. (16). (b) Maximum height of a settling flexible fiber at different fiber flexibilities, normalized by half the fiber length, at  $\text{Ga} = 40$ , and comparisons to the models of Marchetti *et al.* [13].

flexible fibers, respectively. To cover both dilute and semidilute regimes (see, e.g., the definitions of Herzhaft and Guazzelli [22]), we vary the number density  $nL^3$  from 0.5, representing the dilute regime  $n(L/2)^3 < 1$  (see [22]), to 25, representing semidilute regimes  $1 < n(L/2)^3 < L/d = r_p$  (see [22]). The domain size in the settling direction is chosen to be twice as long as those in the horizontal directions. Periodic boundary conditions are applied in all three directions. We also repeated some of our simulations in a domain twice as big as the one detailed in Table II and did not find any significant change in the average settling velocity or the number of the streamers formed per width of the box by the settling fibers. Potential effects of the box size on the structure of the streamers have been discussed by Metzger *et al.* [25] and Saintillan *et al.* [24].

The results of our code have been validated previously for the rotations of a rigid fiber in a shear flow and oscillations of a single hanging flexible fiber under gravity without flow [40]. Here we validate our numerical approach for the settling of a single rigid and flexible fiber in a Stokes flow. For rigid fibers, we compare our numerical simulations of the settling of a single fiber with different initial angles against the solution of Batchelor [6] and Mackaplow and Shaqfeh [7] using a slender body approximation,

$$w_{\text{vis}} = \frac{\text{Ga}}{16r_p^2} \left[ (\ln 2r_p + 0.193) \frac{\mathbf{g}}{g} + (\ln 2r_p - 1.807) \left( \mathbf{p} \cdot \frac{\mathbf{g}}{g} \right) \mathbf{p} \right], \quad (16)$$

where  $w_{\text{vis}}$  is the analytical solution for the settling velocity normalized by  $U_s$  and  $\mathbf{p}$  is a unit vector in the fiber direction (indicated by the fiber end-to-end direction here). For this validation, we simulated the settling of a rigid fiber at  $\text{Ga} = 1$  and  $r = 0.14$ . Therefore, for our fiber aspect ratio of  $r_p = 20$ ,  $w_{\text{vis}}$  should range between  $6.1 \times 10^{-4}$  for a horizontal rigid fiber to  $9 \times 10^{-4}$  for a vertical rigid fiber. The averaged settling velocity in the statistically steady state versus different angles of the fiber with the gravity direction  $\theta$  are depicted in Fig. 1(a). Our numerical results follow the decreasing trend of the analytical solution of  $w_{\text{vis}}$  with increasing  $\theta$  closely, with the largest difference being less than 5%.

For flexible fibers, we compare our results for the maximum height of a single settling fiber normalized by  $L/2$ ,  $\delta$ , at different fiber flexibilities to the slender body and bead-spring model of Marchetti *et al.* [13]. For these simulations we have chosen  $\text{Ga} = 40$  (estimated from their experimental data),  $r_p = 30$ , and  $r = 0.1$ . The comparisons are presented in Fig. 1(b). Our results are close to both the slender body and the bead-spring model of Marchetti *et al.* [13]. Similar to their

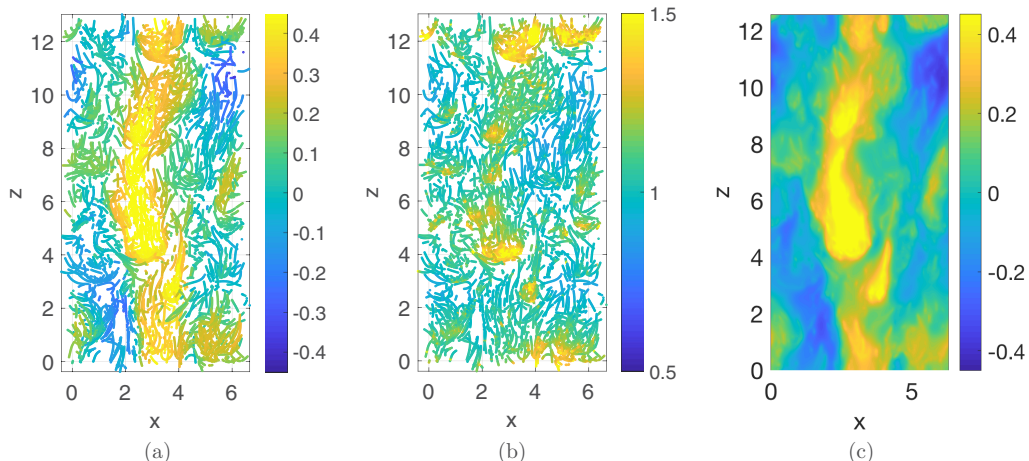


FIG. 2. Snapshots of (a) settling velocities of all fibers in a thin slice in the domain, (b) local concentrations of all fibers in that thin slice, and (c) the corresponding fluid velocity for  $nL^3 = 25$  and  $\gamma = 0.1$ . Positive velocities are in the direction of gravity and negative velocities are in the opposite direction of gravity.

study, our simulations of a single settling flexible fiber reveal that at low fiber flexibility the fiber deformation can be approximated by the slender body theory for weakly flexible fibers, where the fiber height increases linearly with the fiber flexibility. At high fiber flexibility the fibers are almost fully folded and the normalized fiber height approaches 1.

### III. STREAMERS

#### A. Structure of the streamers

Before discussing the settling properties and deformations of the fibers, we examine the formation of streamers in the settling suspension. Streamers are regions of high packing of fibers that are correlated to high local settling velocities [25,54]. The formation of streamers also creates regions of low concentrations of fibers outside the streamers where fibers can move upward in the opposite direction of gravity. Figure 2 shows the snapshots of a slice of the streamers for flexible fibers at the highest number density  $nL^3 = 25$ . A stream of fibers is settling with high velocity in the middle (positive velocities are in the direction of gravity and negative velocities are in the opposite direction of gravity). This region correlates to high velocities in the fluid phase as well. The rest of the fibers either settle at significantly lower velocities or move upward. In the fluid as well, the regions outside the streamers are associated with low or negative velocities. The three-dimensional structure of the streamers is presented in Fig. 3 for rigid and flexible fibers at  $nL^3 = 10$  and 25. The lowest fiber density at which the streamers clearly form is  $nL^3 = 10$ . In this figure the streamers are identified as the fibers with settling velocities  $w > 0.3$  and the fibers in the backflow region are distinguished by  $w < -0.15$ . We recall here that  $w$  is expressed in units of  $U_s = \sqrt{rgL}$ , a measure of the convective settling velocity of a fiber with length  $L$  and density difference ratio  $r$ . Similar to the numerical simulations of Gustavsson and Tornberg [54], in our simulations the structures of the streamers are persistent in time until the fibers on the edges are eroded and dispersed. The streamers did not break down to smaller-scale streamers as observed in some laboratory experiments for rigid fibers [25]. The streamers in Fig. 3 appear as oblique columns of fibers with their vertical connectivity being occasionally lost in some locations. Inside the streamers, clusters of fibers or flocs [54] are created that form the core of the streamers.

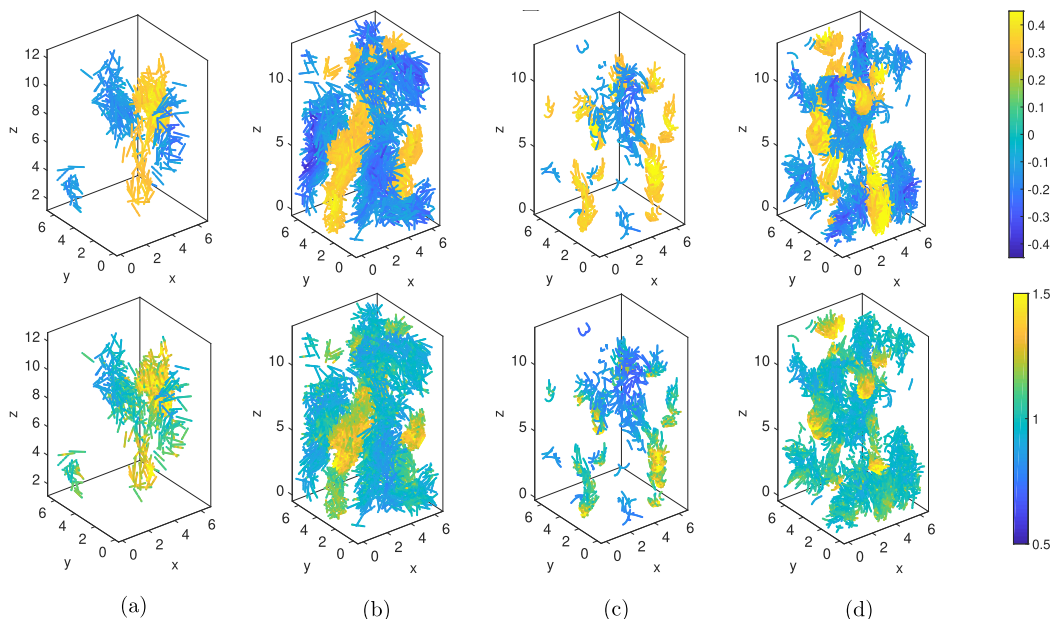


FIG. 3. Snapshots of the streamers and backflow regions for (a)  $\gamma = 20$  and  $nL^3 = 10$ , (b)  $\gamma = 20$  and  $nL^3 = 25$ , (c)  $\gamma = 0.1$  and  $nL^3 = 10$ , and (d)  $\gamma = 0.1$  and  $nL^3 = 25$ . In the top row the fibers are colored by their settling velocity and in the bottom row they are colored by their local fiber concentration  $C$ . Only the fibers with  $w > 0.3$  or  $w < -0.15$  are shown.

To relate the formation of the streamers to the flocs, it is of interest to quantify the local packing of the fibers. For any numerical point  $j$  on a fiber we define a local concentration  $C_j$ ,

$$C_j = \frac{L_x^2}{12N_p} \sum_{i=1, i \neq j}^{N_p} \frac{1}{d_{ij}^2}, \quad (17)$$

where  $N_p$  is the total number of numerical Lagrangian fiber points in a sphere of radius  $L_x/2$  positioned such that the numerical point  $j$  is in its center and  $d_{ij}$  is the distance between the Lagrangian point  $j$  and the Lagrangian points  $i$  in the sphere of radius  $L_x/2$ . The definition of  $C_j$  has been normalized to give 1 if the  $N_p$  Lagrangian points were uniformly distributed in the numerical domain. The local concentrations at numerical points  $C_j$  are averaged over the 21 numerical points on each fiber to give the local concentration  $C$  for each fiber. To evaluate the spatial variations of fiber packing, we also define a three-dimensional version of a radial distribution function (RDF)

$$g(R) = \left( \frac{N_R}{V_R} \right) / \left( \frac{N}{V} \right), \quad (18)$$

where  $N_R$  is the number of pairs of Lagrangian points in a spherical element with radius  $R$  and volume  $V_R$ ,  $N$  is the total number of Lagrangian point pairs in a sphere with radius  $L_x/2$  if all the Lagrangian points were distributed uniformly, and  $V$  is the volume of the sphere with radius  $L_x/2$ . Two-dimensional radial distribution functions have commonly been used to quantify the preferential concentration of point particles in turbulent flows [55,56]. Here we extend the definition of RDFs in these studies to three dimensions and also filter out the bins that correspond to integer multiples of  $L/21$  to remove the bias towards the distances between the Lagrangian points on the same fiber from our RDFs.

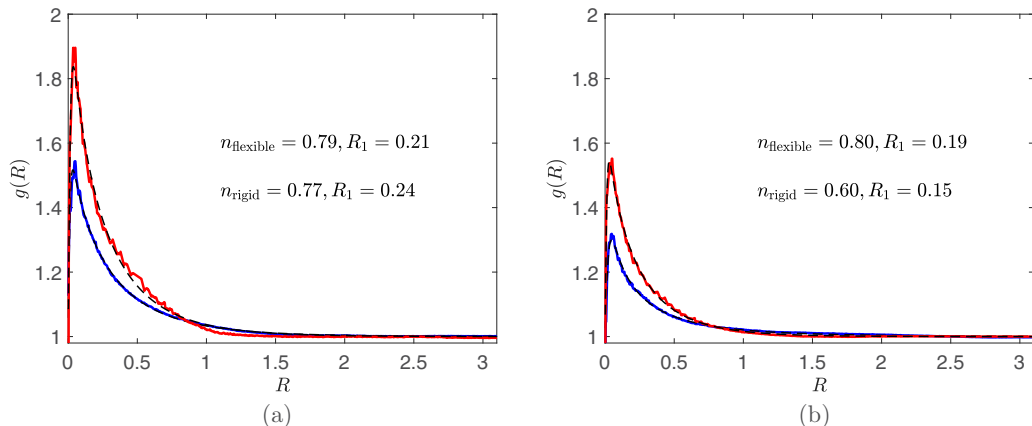


FIG. 4. Radial distribution functions for different fiber concentrations and (a)  $nL^3 = 10$  and (b)  $nL^3 = 25$ . In each panel red shows flexible fibers with  $\gamma = 0.1$  and blue rigid fibers with  $\gamma = 20$ . The black dashed lines show the fits to the RDFs provided by Eq. (19) (note that the fits are sometimes very close to the curves and hardly distinguishable). The parameters  $n$  and  $R_1$  are defined in Eq. (19).

The local concentration  $C$  of the streamers and upward moving fibers are computed for the snapshots in Figs. 2 and 3. In all the cases, the streamers occur in regions of relatively high concentration of fibers and upward moving fibers are associated with low local fiber concentrations. The streamers are formed around cores of highly clumped fibers, the flocs, and the wake regions of these cores. The cores are significantly smaller in the case of flexible fibers where fiber deformations create more packing. To quantify the spatial structure of the streamers, in Fig. 4 we present the RDFs of the four cases discussed in Fig. 3. To each RDF we fit a function of the form

$$g(R) \sim A \tanh\left(\frac{R}{R_0}\right) \exp\left(\frac{-R}{R_1}\right)^n + 1, \quad (19)$$

where  $A$  is a measure of the peak value,  $R_0$  identifies the location of the peak in the RDF (set by the mesh size),  $R_1$  gives a measure of the length scale of the flocs in the core, and  $n$  measures the rate of decay of the core of the streamer. This function provides a good fit to the RDFs. The peaks in the RDFs are higher for flexible fibers and also for lower  $nL^3$ . So, as can also be seen qualitatively in Fig. 3, flexible fibers and lower number density fiber suspensions have higher maximum packings in the streamers. Higher packings in the case of flexible fibers are due to their deformation and in the case of a lower number density suspension due to their higher mobility. The decay rates  $n$  and the floc length scales  $R_1$  are similar in all the cases except for the rigid fibers at  $nL^3 = 25$ . This indicates that the streamers reach a self-similar structure for all the cases except when the mobility of rigid fibers is significantly limited at  $nL^3 = 25$ . In this case, the fiber floc length scale is smaller and the decay rate of the core of the streamers is lower, both indicating a weaker formation of the streamers due to limited fiber mobility.

### B. Velocity-concentration correlations

The correlations between the settling velocity  $w$  and the local concentration of fibers  $C$  for individual fibers is shown in Fig. 5. These data are collected from all fibers at four instants in the statistically stable state in each case. The  $w$ - $C$  plane is divided into four quadrants by the averages of the settling velocity and local fiber concentration. The first quadrant with high fiber settling velocity and high local concentrations contains the streamers and the third quadrant with negative velocities and low local fiber concentrations mainly consists of fibers in the backflow regions. The other two quadrants represent the fibers that are in the boundaries between these two regions. For each case

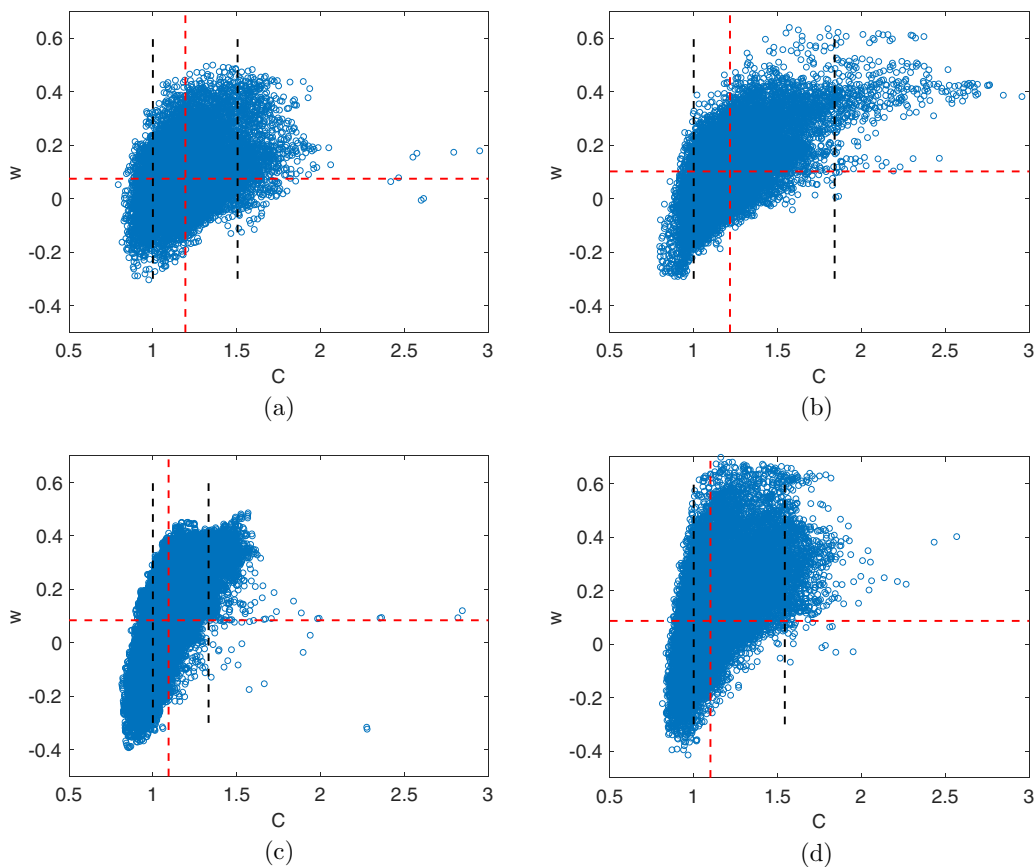


FIG. 5. Scatter plots of the fiber settling velocity versus the local fiber concentration  $C$  for (a)  $\gamma = 20$  and  $nL^3 = 10$ , (b)  $\gamma = 0.1$  and  $nL^3 = 10$ , (c)  $\gamma = 20$  and  $nL^3 = 25$ , and (d)  $\gamma = 0.1$  and  $nL^3 = 25$ . The red dashed lines are the averages of  $w$  and  $C$  over all fibers. The black dashed lines show the minimum and maximum of the RDF for each case.

we also identify a lower and an upper bound for  $C$ , where the lower bound  $C_{\min} = 1$  corresponds to a uniform distribution of fibers and the upper bound  $C_{\max}$  is the maximum of the RDF for that case.

While the highest settling velocities in Fig. 5 do not always correspond to the highest local concentrations, from Fig. 3 it can be conjectured that they always occur near a region of highly packed fibers and are caused by the drag of these highly concentrated fibers. Flexible fibers, compared to rigid fibers, achieve higher settling velocities in the first quadrants due to higher packings in the streamers and also their ability to deform and streamline the flow [37,38]. The upward moving fibers in the third quadrants, however, show little sensitivity to the fiber flexibility. By increasing  $nL^3$  from 10 to 25, the local concentrations of fibers in the streamers and the upper bounds on  $C$  decrease as the mobility of fibers becomes limited. The maximum settling velocity of the streamers is however less influenced by  $nL^3$  since the strong hydrodynamic and fiber-fiber interactions compensate for the limited mobility and maximum packing at higher  $nL^3$ . The upward moving fibers benefit from these interactions and attain higher velocities at higher  $nL^3$ . Rigid fibers at  $nL^3 = 25$  exhibit a considerably narrower range of concentrations as they are highly immobile and their streamers are the most weakly formed.

To build a more direct correlation between the settling velocity and local concentration, we average the settling velocities of individual fibers in Fig. 5 over bins of  $C$  to give bin-averaged

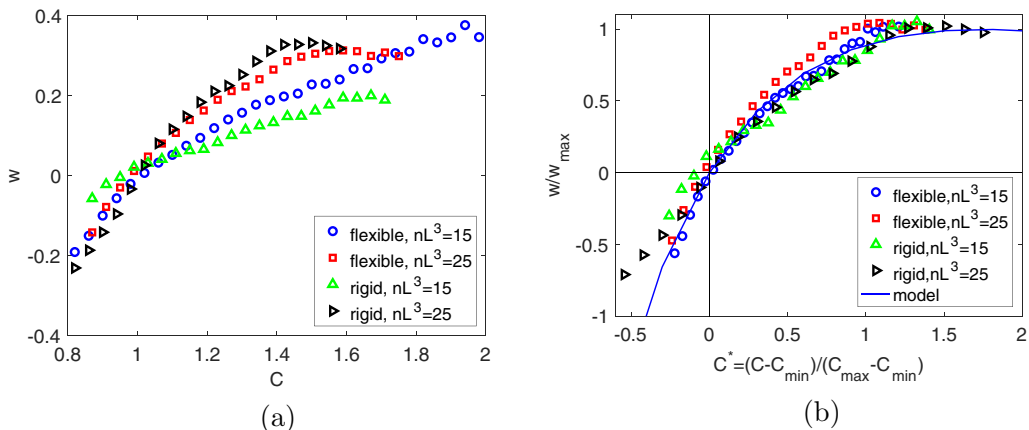


FIG. 6. Dependence of  $w$  on  $C$  from the bin-averaged data in Fig. 5: (a) raw data and (b)  $C$  and  $w$  normalized.

$w$  versus  $C$ , as presented in Fig. 6. The size of the bins in each case is 0.04. This bin size is the smallest value that gives a smooth bin-averaged  $w$  function and further decreasing of the bin size does not significantly change the shape of the averaged function. The bin-averaged settling velocities for both flexible and rigid fibers show a monotonically increasing trend with increasing concentrations. For all the cases, a zero crossing occurs close to  $C = C_{\min} = 1$  [see Fig. 6(a)]. By normalizing the settling velocity by its maximum and introducing a normalized local concentration  $C^* = (C - C_{\min}) / (C_{\max} - C_{\min})$ , all curves collapse and the zero crossings occur at  $C^* = 0$  [see Fig. 6(b)]. This leads us to the conclusion that the settling velocity of individual fibers in semidilute suspensions is highly dependent on the clumping of the fibers. In regions where the local concentration is lower than the uniform concentration, the fibers move on average in the opposite direction of gravity. In regions where the fibers are clumped together, the fibers' velocity depends on  $C^*$ , which measures how much the concentration is higher than the uniform concentration compared to the statistical maximum range of concentrations in the suspension. As  $C^*$  increases, the clump of fibers gets heavier and it settles faster. The settling velocities, however, saturate for  $C^* > 1$ , where the fluid that can flow through the network of fibers experiences low permeability. Using Darcy's law for permeability, the settling velocity of fibers in the suspension can be modeled as

$$w = Gak^*(C)C^*, \quad (20)$$

where  $k^*$  is a dimensionless permeability as a function of the local concentration  $C$ . This model states that the fibers settle in the direction of gravity for  $C^* > 0$ , where the local density is higher than the average density of the suspension. The settling velocity of the fibers increases almost linearly with increasing  $C^*$  as the clumps get heavier and the local density of the suspension increases. However, as the fibers are more packed, the permeability drops and the resistance against the fluid going through the fiber increases. Here we choose a permeability model similar to the functional form introduced by Hewitt *et al.* [57], which is more suitable for low volume fractions (note that our volume fractions are less than 0.05),

$$k^*(C) = \frac{\mathcal{A}}{C} \ln\left(\frac{\mathcal{N}C_{\min}}{C}\right) \exp\left(-\frac{C}{C_{\max}}\right). \quad (21)$$

The parameters  $\mathcal{A}$  and  $\mathcal{N}$  in this model are constants that measure the scaling of permeability and the ratio between maximum and uniform fiber packing, respectively. These parameters are found from fits to the numerical data. Figure 6(b) plots the modeled settling velocity as a function of  $C^*$  from Eqs. (20) and (21) with  $\mathcal{A} = 0.01$  and  $\mathcal{N} = 10$ . The model closely follows the increasing trend

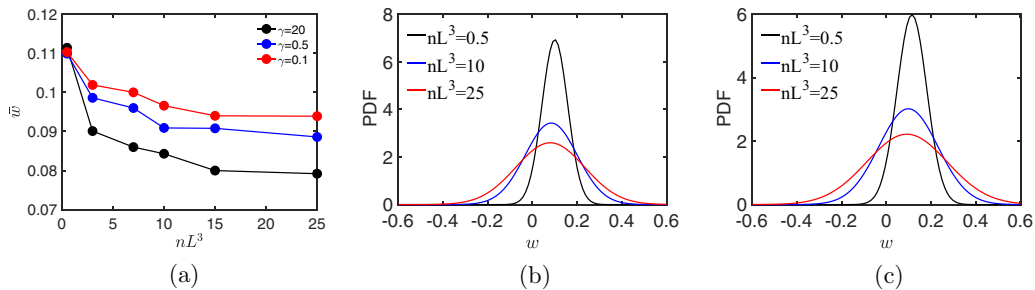


FIG. 7. (a) Averaged settling velocity of all fibers in the statistically steady state versus different fiber number density for different values of bending rigidity  $\gamma$ , (b) PDFs of settling velocity for rigid fibers ( $\gamma = 20$ ) at different fiber number density, and (c) PDFs of settling velocity for the most flexible fibers ( $\gamma = 0.1$ ) at different fiber number density.

of  $w$  from  $C^* = -0.25$  to  $C^* = 1$  and the saturation of  $w$  for  $C^* > 1$  (or  $C > C_{\max}$ ). The agreement between the model and the numerical results confirms our earlier conjecture that the clumped fibers settle faster due to the higher local density of the suspension, until a local concentration of  $C_{\max}$ , measured by the maxima of the RDFs, is reached. At this concentration the reduction in permeability balances the increase in local density. The determined parameter  $\mathcal{A} = 0.01$  is of the same order of magnitude as  $1/Ga = 0.0063$ , which indicates that  $Ga$  can be combined with the constant  $\mathcal{A}$  in the permeability relation to get a scaling constant closer to unity. The obtained value of  $\mathcal{N} = 10$  suggests that the maximum packing of fibers is close to 10 times the uniform fiber concentration in each case. According to the definition of Herzhaft and Guazzelli [22], our fiber suspensions become concentrated for  $nL^3 \sim 160$ , which is 6–11 times higher than the  $nL^3$  of the cases shown in Fig. 6. These predictions for the values corresponding to a concentrated suspension are close to the fitted ratio  $\mathcal{N} = 10$ .

#### IV. SETTLING AND DRIFT VELOCITY

The mean settling velocity for different number density and bending rigidities is shown in Fig. 7(a). For each bending rigidity  $\gamma$ , the mean settling velocity decreases with increasing fiber number density due to the hindering effect by the adjacent fibers. The mean settling velocity increases with increasing fiber flexibility. At a very low fiber number density of  $nL^3 = 0.5$ , however, the mean settling velocity does not depend on fiber flexibilities. In this case, while fiber deformations and streamlining of the flow in flexible fibers are expected to reduce the fiber drag force [37,38] (based on studies for fibers with fixed orientations), the higher reorientation of flexible fibers with the horizontal direction (as will be seen in Sec. V) increases the drag force. At higher  $nL^3$ , fiber flexibility enhances fiber packing and contributes to higher settling velocities. In addition, since the fiber orientations for rigid and flexible fibers become closer at higher  $nL^3$ , the effect of drag reduction for more flexible fibers is more pronounced in enhancing the settling velocity for  $nL^3 > 3$ . The formation of the streamers for  $nL^3 > 10$  plays an important role in settling of the fibers. The streamers create dense clumps of fibers that settle rapidly and counterbalance the effects of hindering so that the mean settling velocities reach a plateau for  $nL^3 > 15$ . As discussed in the preceding section, the streamers create higher packings in flexible fibers. Therefore, the difference between the mean settling velocity of flexible and rigid fibers is more pronounced at higher  $nL^3$ .

The probability density functions (PDFs) of the settling velocities for rigid and flexible fibers are shown in Figs. 7(b) and 7(c). The deviation from the mean settling velocity increases by increasing the fiber number density due to the fiber-fiber interactions and fiber packing. The settling velocities also have slightly broader PDFs for flexible fibers compared to rigid fibers. In a dilute regime  $nL^3 = 0.5$ , the deformations of individual fibers and their reorientations due to the interactions with the

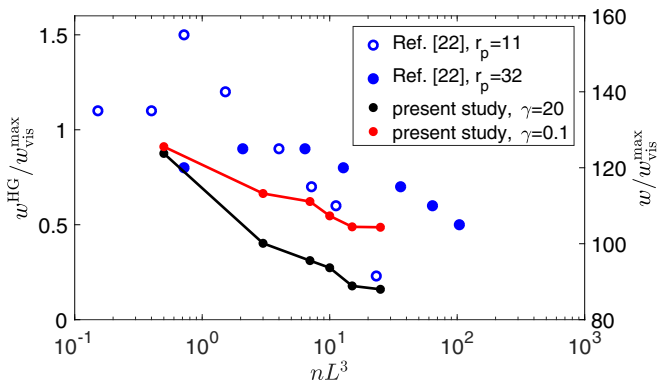


FIG. 8. Comparison of the mean settling velocity normalized by the settling velocity of an isolated vertical fiber in a Stokes flow from the present study (plotted on the right axis) to the experimental measurements of Herzhaft and Guazzelli [22] in a Stokes flow (plotted on the left axis).

flow create variations in the fiber settling velocity. In the denser regimes, the interactions of fibers with their neighboring fibers in fiber-packed regions contribute to larger variations of the settling velocities from the mean.

For the settling of rigid fibers in a Stokes flow, Herzhaft and Guazzelli [22] identified a dilute and a semidilute regime in their experiments. In the dilute regime, the clumping of the fibers results in more alignment with the direction of gravity and fibers settling even faster than the Stokes velocity of an isolated fiber. In the semidilute regime, their experiments revealed hindered settling velocities as the clumping effects became less significant. In Fig. 8 we compare our settling velocities for the rigid and most flexible fibers against the results of Herzhaft and Guazzelli [22] for fiber aspect ratios of  $r_p = 11$  and  $r_p = 32$ . Our fiber aspect ratio of 20 falls between these two values. The settling velocities of our inertial fibers are two orders of magnitude higher than the Stokes velocity of an isolated rigid fiber with the same aspect ratio settling vertically.

In the dilute regime, i.e.,  $nL^3 < 10$ , our settling velocities are hindered when increasing  $nL^3$  from 0.5 to 10. In the semidilute regime  $nL^3 > 10$ , where the streamers start to form, the hindering of fiber velocity slows down for our inertial fibers. This is the opposite of the experimental observations of Herzhaft and Guazzelli [22], where the fibers' velocity was significantly hindered in their semidilute regime (they identified  $nL^3 > 8$  as semidilute). This comparison suggests that, contrary to the viscous settling of fibers, in inertial settling of fibers, the streamers form at semidilute fiber concentrations and significant hindering of settling velocities occurs in dilute regimes. It is however possible that the structure of the streamers starts to weaken at denser fiber concentrations (as we observed for rigid fibers at  $nL^3 = 25$ ) and the settling of fibers is significantly hindered again. Moreover, as we observed for local fiber clumps, the permeability of the fiber suspension decreases for very high fiber number densities. This reduced permeability is also likely to lower the mean settling velocity of the fibers for  $nL^3 > 25$ . Performing these high fiber concentrations however requires a significant amount of computational time and is beyond the scope of the present study.

The mean amplitude of the root mean square (rms) of the horizontal velocity components (perpendicular to the gravity direction) of the fibers is presented in Fig. 9 for different bending rigidities and number densities. The amplitude of the rms of the horizontal velocity increases monotonically with  $nL^3$ , but does not show a significant dependence on fiber flexibility. When the horizontal velocities are normalized with respect to the average settling velocity, as shown in Fig. 9(b), we note that the horizontal velocities relative to settling velocities are lower for more flexible fibers. At lower concentrations, the horizontal velocities are due to the chaotic nature of settling of fibers in inertial regimes and also fiber-fiber interactions. At higher concentrations, we attribute the horizontal velocities to the formation of streamers and their meandering structure as

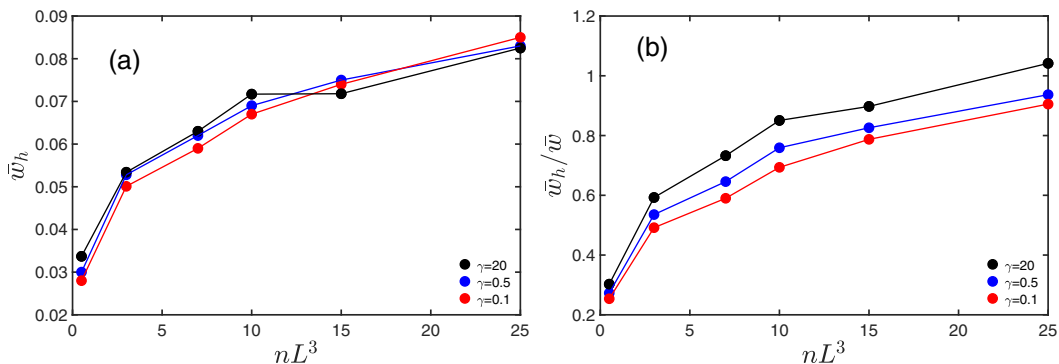


FIG. 9. Averaged horizontal velocity amplitude (rms) of fibers in the statistically steady state versus different fiber number densities for different values of bending rigidity  $\gamma$ . The average horizontal velocities are scaled by (a) the characteristic convective velocity  $U_s$ , and (b) the settling velocity in each case.

they settle. As fibers drift more horizontally relative to their settling velocity at lower flexibility [8] and the stramer's meandering effects are stronger for rigid fibers due to their lower packing [see Fig. 3(b)], the rigid fibers show higher mean horizontal velocities compared to their averaged settling velocity, while their absolute horizontal velocities are the same as those of the flexible fibers. For higher  $nL^3$ , where the streamers are formed, the values of horizontal velocities are comparable to the average settling velocities. However, the increasing trend of the horizontal velocities with  $nL^3$  exhibits a smaller slope for  $nL^3 > 10$ , indicating that the fibers' horizontal mobility is limited at higher fiber number densities.

The PDFs of the horizontal velocity in Fig. 10 show that the variations in the horizontal velocity increase with increasing number density. The maximum horizontal velocities reached by the fibers continue to increase with  $nL^3$  even at  $nL^3 = 25$ . This indicates that even though the fiber mobility is limited at this high fiber number density, the interactions between the fibers can still enhance their local horizontal motion. The PDF of the horizontal velocity is slightly broader for rigid fibers compared to flexible fibers at  $nL^3 = 0.5$ . This indicates that the rigid fibers can reach higher horizontal velocities as they do not experience the reorienting torque as in the case of flexible fibers.

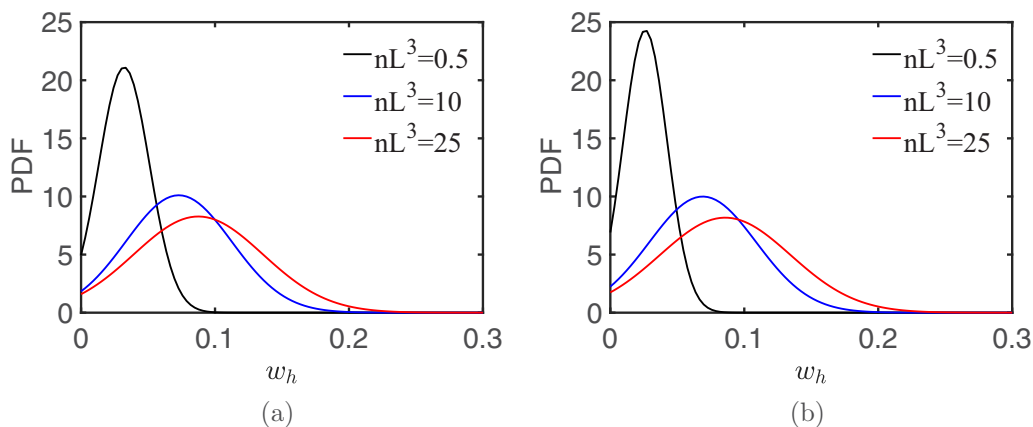


FIG. 10. PDFs of the horizontal velocity amplitude (rms) for (a) rigid ( $\gamma = 20$ ) and (b) flexible ( $\gamma = 0.1$ ) fibers.

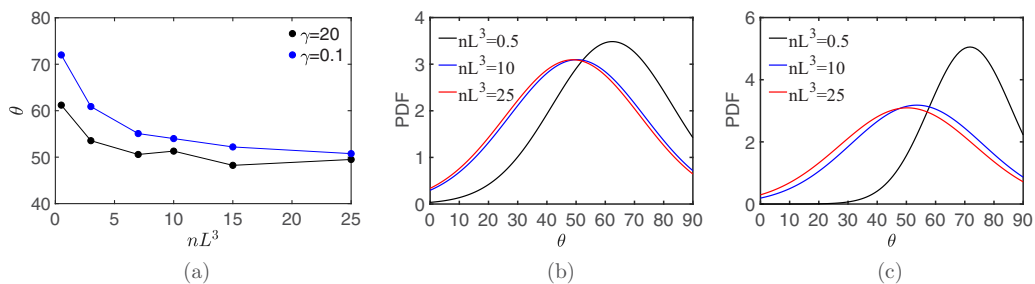


FIG. 11. (a) Averaged orientation of all fibers in the statistically steady state versus different fiber number density for different values of bending rigidity  $\gamma$ . Also shown are the PDFs of the angle between the fibers and the gravity direction for (b) rigid ( $\gamma = 20$ ) and (c) flexible ( $\gamma = 0.1$ ) fibers.

In denser regimes, where fiber packing becomes more important, the PDFs are no longer sensitive to the fiber flexibility.

## V. ORIENTATION AND BENDING

Figure 11 shows the means and PDFs of the orientation of the fibers with respect to the gravity direction and Fig. 12 delineates the means and PDFs of the fiber end-to-end distance normalized by the fiber length  $L$ , a measure of fiber deformation for flexible fibers. For the flexible fibers, the orientation is defined as the angle a line connecting the two ends of the fibers makes with the gravity direction. Figures 11 and 12 show that for  $nL^3 > 7$ , as the suspensions transition from dilute to semidilute regimes and fiber mobility becomes limited, the fiber orientations and deformations become insensitive to the fiber number density.

At a very low concentration of  $nL^3 = 0.5$ , both flexible and rigid fibers are on average more oriented toward the horizontal plane and perpendicular to the gravity direction, which is the stable state of flexible fibers in a Stokes flow [9,12]. As  $nL^3$  increases, the fibers become more inclined to the gravity direction due to the shear rate generated by the fiber-fiber interactions and the streamers. The PDFs of the orientations show larger variations in the fiber angle in semidilute compared to dilute suspensions due to the stronger fiber-fiber interactions. The PDFs of fiber orientations, however, are not sensitive to the fiber concentration in semidilute regimes as the fiber mobility is limited. In both dilute and semidilute regimes, flexible fibers are on average more aligned with the

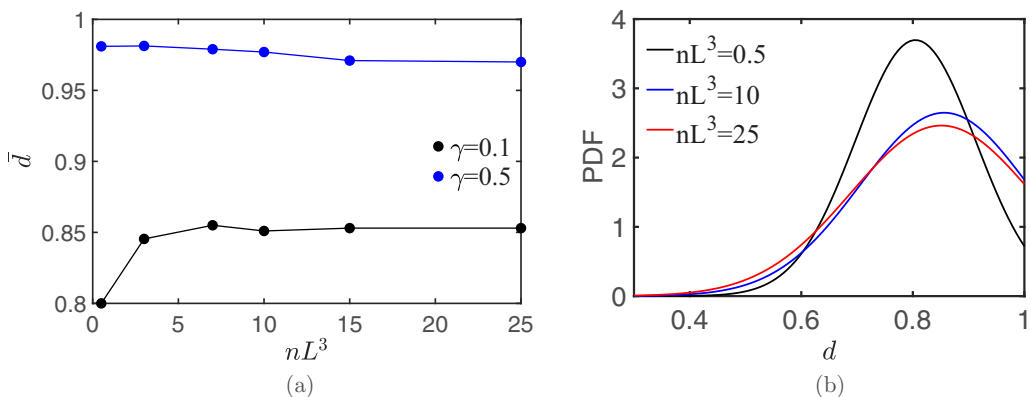


FIG. 12. (a) Mean end-to-end distance scaled by the fiber length  $L$  and (b) PDFs of the end-to-end distance scaled by  $L$  for flexible fibers with  $\gamma = 0.1$ .

direction perpendicular to the gravity (horizontal direction) compared to the rigid fibers. In dilute regimes, flexible fibers experience re-orienting torque that aligns them with the horizontal plane direction, similar to the findings in a Stokes flow [12]. In semidilute regimes, while the fibers are more aligned with the gravity direction due to the hydrodynamic interactions with other fibers, they are still slightly more horizontal compared to their rigid fiber counterparts.

In Fig. 12, by increasing the fiber concentration beyond  $nL^3 = 0.5$ , the deformation of weakly flexible fibers is enhanced, but the deformation of moderately flexible fibers diminishes. For  $\gamma = 0.5$ , i.e., weakly flexible fibers with small fiber deformations, the mean end-to-end distance decreases slightly when the suspension transitions from a dilute to a semidilute regime. In this case the fiber-fiber interactions induce more fiber bending. For  $\gamma = 0.1$ , i.e., moderately flexible fibers with larger fiber deformations, however, the fiber-fiber interactions at higher  $nL^3$  in the semidilute range create more isotropic stresses on the fiber and straighten the fibers that are bent under gravitational forces. For  $nL^3 > 7$ , the limited fiber mobility and higher fiber packing in the streamers hamper this effect and the mean end-to-end distance remains constant. For  $\gamma = 0.1$ , the PDFs of the fiber deformations show little sensitivity to the fiber number density for  $nL^3 > 10$ . Due to the limited fiber mobility, the number of fully straight fibers, i.e.,  $d = 1$ , has significantly increased from  $nL^3 = 0.5$  to  $nL^3 = 10$ .

## VI. CONCLUSION

In the present study we have examined the settling of a suspension of flexible and rigid fibers in dilute and semidilute regimes using an immersed boundary method for the coupling between the fluid and solid phase. We have considered an inertial regime with  $Ga = 160$  and a single fiber aspect ratio of  $r = 20$ . This paper extends the previous research on the settling of fiber suspensions to flexible fibers and also to inertial regimes.

We have found that for  $nL^3 > 10$  the formation of the streamers and the packing of the fibers inside the streamers play an important role in determining the settling behavior of the fiber suspension. By examining the structure of the streamers and defining a local fiber concentration parameter, we have shown that the streamers are formed in the regions of highly packed fibers and their wakes. By increasing the fiber number density, both flexible and rigid fibers exhibit lower packing in the streamers as their mobility becomes limited. As shown by their radial distribution function, flexible fibers maintain a self-similar structure at higher  $nL^3$ . Rigid fibers, on the other hand, show lower packings in the streamers compared to the flexible fibers and their streamers' structure is weakened at higher  $nL^3$ .

We have examined the correlations between the settling velocity of an individual fiber in the suspension and the local concentration of that fiber. The fastest settling fibers are generally correlated to high local concentrations. The fastest upward moving fibers are found mostly where the local concentration is lower than that of a uniform distribution. By bin averaging the settling velocity of individual fibers in successive local concentration intervals, we obtained a monotonically increasing bin-averaged velocity as a function of the local concentration. We showed that the relationship between the bin-averaged velocity and the local concentration collapses for all data sets if proper normalizations are applied. We thus proposed a model for the normalized settling velocity of the fibers versus the normalized local concentration. In summary, the model states that on average fibers move upward if their local concentration is less than the uniform distribution. For local concentrations higher than the uniform distribution, the fibers settle on average and their settling velocity increases as the fibers clump more. For local concentrations higher than a maximum statistical concentration in the suspension, found as the maximum of the RDFs, the settling velocity saturates as the reduced permeability in the clump creates a significant resistance against the fluid.

The average settling velocity of the suspension increases by increasing the fiber flexibility, except for the  $nL^3 = 0.5$  case. We attribute this to the ability of the flexible fibers to streamline the flow and also to create higher packings in the streamers. While the average settling speed of both rigid and flexible fiber suspensions was hindered in the dilute regime ( $0.5 < nL^3 < 10$ ), the hindering

effects were counterbalanced by the formation of the streamers in the semidilute regime ( $nL^3 > 10$ ). This finding is contrary to the findings of Herzhaft and Guazzelli [22] in a Stokes flow, where the streamers structure started to break down in the semidilute regime, leading to the significant hindering of the suspension velocity. The rms of the horizontal velocities of the fibers increase monotonically (although with a smaller slope for  $nL^3 > 10$ ) with increasing fiber concentration for both rigid and flexible fibers. In addition, flexible fibers have lower ratios of horizontal to settling velocities compared to flexible fibers, which we attribute to the reorienting torque and higher fiber packings in the case of flexible fibers.

We measured the limited mobility of the fibers at higher  $nL^3$  by examining the fiber rotation and deformation. The means and PDFs of these parameters exhibit a small dependence on the fiber number density for  $nL^3 > 7$  and  $nL^3 > 10$ , respectively. These indicate that the fiber mobility becomes limited when the suspensions transition from a dilute to a semidilute regime. The fibers are on average more inclined toward the horizontal direction in dilute regimes. In semidilute regimes, the fibers orient themselves slightly more toward the vertical direction as the fiber-fiber interaction are more important and streamers are formed. In both regimes, flexible fibers are inclined more to the horizontal direction compared to the rigid fibers. Through the transition from dilute to semidilute, the weakly flexible fibers were deformed more. Moderately flexible fibers, however, were less deformed in semidilute regimes compared to dilute regimes.

For future work, adding frictional forces to the fibers, a more comprehensive investigation of the transition from viscous to inertial regimes, and studying strongly flexible fibers are research directions that can be explored. In addition, it is of great interest to understand how the structure of the streamers evolves in concentrated regimes.

#### ACKNOWLEDGMENTS

A.A.B. and L.B. have been supported by the European Research Council Grant No. ERC-2013-CoG-616186, TRITOS. The authors are thankful to anonymous reviewers for insightful comments that helped improve the quality of this work. The authors acknowledge computer time provided by Swedish National Infrastructure for Computing.

- 
- [1] N. Provatas, M. J. Alava, and T. Ala-Nissila, Density correlations in paper, *Phys. Rev. E* **54**, R36 (1996).
  - [2] M. Kamali and Z. Khodaparast, Review on recent developments on pulp and paper mill wastewater treatment, *Ecotoxicol. Environ. Saf.* **114**, 326 (2015).
  - [3] D. W. Cooper, Particulate contamination and microelectronics manufacturing: An introduction, *Aerosol Sci. Technol.* **5**, 287 (1986).
  - [4] L. Jiang, L. Gao, and J. Sun, Production of aqueous colloidal dispersions of carbon nanotubes, *J. Colloid Interface Sci.* **260**, 89 (2003).
  - [5] A. J. Gooday and C. M. Turley, Responses by benthic organisms to inputs of organic material to the ocean floor: A review, *Philos. Trans. R. Soc. London Ser. A* **331**, 119 (1990).
  - [6] G. K. Batchelor, Slender-body theory for particles of arbitrary cross-section in Stokes flow, *J. Fluid Mech.* **44**, 419 (1970).
  - [7] M. B. Mackaplow and E. S. G. Shaqfeh, A numerical study of the sedimentation of fibre suspensions, *J. Fluid Mech.* **376**, 149 (1998).
  - [8] L. Li, H. Manikantan, D. Saintillan, and S. E. Spagnolie, The sedimentation of flexible filaments, *J. Fluid Mech.* **735**, 705 (2013).
  - [9] X. Xu and A. Nadim, Deformation and orientation of an elastic slender body sedimenting in a viscous liquid, *Phys. Fluids* **6**, 2889 (1994).
  - [10] B. Delmotte, E. Climent, and F. Plouraboué, A general formulation of Bead models applied to flexible fibers and active filaments at low Reynolds number, *J. Comput. Phys.* **286**, 14 (2015).

- [11] M. C. Lagomarsino, I. Pagonabarraga, and C. P. Lowe, Hydrodynamic Induced Deformation and Orientation of a Microscopic Elastic Filament, *Phys. Rev. Lett.* **94**, 148104 (2005).
- [12] I. Llopis, I. Pagonabarraga, M. C. Lagomarsino, and C. P. Lowe, Sedimentation of pairs of hydrodynamically interacting semiflexible filaments, *Phys. Rev. E* **76**, 061901 (2007).
- [13] B. Marchetti, V. Raspa, A. Lindner, O. du Roure, L. Bergougnoux, E. Guazzelli, and C. Duprat, Deformation of a flexible fiber settling in a quiescent viscous fluid, *Phys. Rev. Fluids* **3**, 104102 (2018).
- [14] G. Saggiorato, J. Elgeti, R. G. Winkler, and G. Gompper, Conformations, hydrodynamic interactions, and instabilities of sedimenting semiflexible filaments, *Soft Matter* **11**, 7337 (2015).
- [15] X. Schlagberger and R. R. Netz, Orientation of elastic rods in homogeneous Stokes flow, *Europhys. Lett.* **70**, 129 (2005).
- [16] O. du Roure, A. Lindner, E. N. Nazockdast, and M. J. Shelley, Dynamics of flexible fibers in viscous flows and fluids, *Annu. Rev. Fluid Mech.* **51**, 539 (2019).
- [17] A.-K. Tornberg and M. J. Shelley, Simulating the dynamics and interactions of flexible fibers in Stokes flows, *J. Comput. Phys.* **196**, 8 (2004).
- [18] J. K. Wiens and J. M. Stockie, Simulating flexible fiber suspensions using a scalable immersed boundary algorithm, *Comput. Methods Appl. Mech. Eng.* **290**, 1 (2015).
- [19] N. Quennouz, M. Shelley, O. du Roure, and A. Lindner, Transport and buckling dynamics of an elastic fibre in a viscous cellular flow, *J. Fluid Mech.* **769**, 387 (2015).
- [20] Y.-N. Young and M. J. Shelley, Stretch-Coil Transition and Transport of Fibers in Cellular Flows, *Phys. Rev. Lett.* **99**, 058303 (2007).
- [21] V. Kantsler and R. E. Goldstein, Fluctuations, Dynamics, and the Stretch-Coil Transition of Single Actin Filaments in Extensional Flows, *Phys. Rev. Lett.* **108**, 038103 (2012).
- [22] B. Herzhaft and É. Guazzelli, Experimental study of the sedimentation of dilute and semi-dilute suspensions of fibres, *J. Fluid Mech.* **384**, 133 (1999).
- [23] J. E. Butler and E. S. G. Shaqfeh, Dynamic simulations of the inhomogeneous sedimentation of rigid fibres, *J. Fluid Mech.* **468**, 205 (2002).
- [24] D. Saintillan, E. Darve, and E. S. G. Shaqfeh, A smooth particle-mesh Ewald algorithm for Stokes suspension simulations: The sedimentation of fibers, *Phys. Fluids* **17**, 033301 (2005).
- [25] B. Metzger, É. Guazzelli, and J. E. Butler, Large-Scale Streamers in the Sedimentation of a Dilute Fiber Suspension, *Phys. Rev. Lett.* **95**, 164506 (2005).
- [26] J. Salmela, D. M. Martinez, and M. Kataja, Settling of dilute and semidilute fiber suspensions at finite Re, *AIChE J.* **53**, 1916 (2007).
- [27] H. Manikantan, L. Li, S. E. Spagnolie, and D. Saintillan, The instability of a sedimenting suspension of weakly flexible fibres, *J. Fluid Mech.* **756**, 935 (2014).
- [28] H. Manikantan and D. Saintillan, Effect of flexibility on the growth of concentration fluctuations in a suspension of sedimenting fibers: Particle simulations, *Phys. Fluids* **28**, 013303 (2016).
- [29] C. G. Joung, N. Phan-Thien, and X. J. Fan, Direct simulation of flexible fibers, *J. Non-Newtonian Fluid Mech.* **99**, 1 (2001).
- [30] L. H. Switzer and D. J. Klingenberg, Flocculation in simulations of sheared fiber suspensions, *Int. J. Multiphase Flow* **30**, 67 (2004).
- [31] L. H. Switzer III and D. J. Klingenberg, Rheology of sheared flexible fiber suspensions via fiber-level simulations, *J. Rheol.* **47**, 759 (2003).
- [32] D. Kunhappan, B. Harthong, B. Chareyre, G. Balarac, and P. J. J. Dumont, Numerical modeling of high aspect ratio flexible fibers in inertial flows, *Phys. Fluids* **29**, 093302 (2017).
- [33] D. Dotto and C. Marchioli, Orientation, distribution, and deformation of inertial flexible fibers in turbulent channel flow, *Acta Mech.* **230**, 597 (2019).
- [34] C. Brouzet, G. Verhille, and P. Le Gal, Flexible Fiber in a Turbulent Flow: A Macroscopic Polymer, *Phys. Rev. Lett.* **112**, 074501 (2014).
- [35] M. E. Rosti, A. A. Banaei, L. Brandt, and A. Mazzino, Flexible Fiber Reveals the Two-Point Statistical Properties of Turbulence, *Phys. Rev. Lett.* **121**, 044501 (2018).
- [36] F. Lundell, L. D. Söderberg, and P. H. Alfredsson, Fluid mechanics of papermaking, *Annu. Rev. Fluid Mech.* **43**, 195 (2011).

- [37] S. Alben, M. Shelley, and J. Zhang, How flexibility induces streamlining in a two-dimensional flow, *Phys. Fluids* **16**, 1694 (2004).
- [38] L. Zhu and C. S. Peskin, Drag of a flexible fiber in a 2D moving viscous fluid, *Comput. Fluids* **36**, 398 (2007).
- [39] R. E. Khayat and R. G. Cox, Inertia effects on the motion of long slender bodies, *J. Fluid Mech.* **209**, 435 (1989).
- [40] A. A. Banaei, M. E. Rosti, and L. Brandt, Numerical study of filament suspensions at finite inertia, *J. Fluid Mech.* **882**, A5 (2020).
- [41] B. E. Griffith, R. D. Hornung, D. M. McQueen, and C. S. Peskin, An adaptive, formally second order accurate version of the immersed boundary method, *J. Comput. Phys.* **223**, 10 (2007).
- [42] B. E. Griffith and N. A. Patankar, Immersed methods for fluid-structure interaction, *Annu. Rev. Fluid Mech.* **52**, 421 (2019).
- [43] A. M. Słowicka, E. Wajnryb, and M. L. Ekiel-Jeżewska, Dynamics of flexible fibers in shear flow, *J. Chem. Phys.* **143**, 124904 (2015).
- [44] E. Nazockdast, A. Rahimian, D. Zorin, and M. Shelley, A fast platform for simulating semi-flexible fiber suspensions applied to cell mechanics, *J. Comput. Phys.* **329**, 173 (2017).
- [45] A.-K. Tornberg and K. Gustavsson, A numerical method for simulations of rigid fiber suspensions, *J. Comput. Phys.* **215**, 172 (2006).
- [46] W.-X. Huang, S. J. Shin, and H. J. Sung, Simulation of flexible filaments in a uniform flow by the immersed boundary method, *J. Comput. Phys.* **226**, 2206 (2007).
- [47] A. A. Banaei, J.-C. Loiseau, I. Lashgari, and L. Brandt, Numerical simulations of elastic capsules with nucleus in shear flow, *Eur. J. Comput. Mech.* **26**, 131 (2017).
- [48] R. Mittal and G. Iaccarino, Immersed boundary methods, *Annu. Rev. Fluid Mech.* **37**, 239 (2005).
- [49] A. M. Roma, C. Peskin, and M. J. Berger, An adaptive version of the immersed boundary method, *J. Comput. Phys.* **153**, 509 (1999).
- [50] S. B. Lindström and T. Uesaka, Simulation of semidilute suspensions of non-Brownian fibers in shear flow, *J. Chem. Phys.* **128**, 024901 (2008).
- [51] Y. Yamane, Y. Kaneda, and M. Dio, Numerical simulation of semi-dilute suspensions of rodlike particles in shear flow, *J. Non-Newtonian Fluid Mech.* **54**, 405 (1994).
- [52] J. Kromkamp, D. T. M. van den Ende, D. Kandhai, R. G. M. van der Sman, and R. M. Boom, Shear-induced self-diffusion and microstructure in non-Brownian suspensions at non-zero Reynolds numbers, *J. Fluid Mech.* **529**, 253 (2005).
- [53] Y. Liu, L. Zhang, X. Wang, and W. K. Liu, Coupling of Navier-Stokes equations with protein molecular dynamics and its application to hemodynamics, *Int. J. Numer. Methods Fluids* **46**, 1237 (2004).
- [54] K. Gustavsson and A.-K. Tornberg, Gravity induced sedimentation of slender fibers, *Phys. Fluids* **21**, 123301 (2009).
- [55] M. Rahmani, G. Geraci, G. Iaccarino, and A. Mani, Effects of particle polydispersity on radiative heat transfer in particle-laden turbulent flows, *Int. J. Multiphase Flow* **104**, 42 (2018).
- [56] B. Ray and L. R. Collins, Preferential concentration and relative velocity statistics of inertial particles in Navier-Stokes turbulence with and without filtering, *J. Fluid Mech.* **680**, 488 (2011).
- [57] D. R. Hewitt, D. T. Paterson, N. J. Balmforth, and D. M. Martinez, Dewatering of fibre suspensions by pressure filtration, *Phys. Fluids* **28**, 063304 (2016).